Pore closure in thick aluminum plate: From industrial hot rolling to individual pore observation

P. Gravier, F. Mas, A. Barthelemy, E. Boller, L. Salvo, Pierre Lhuissier

Graphical Abstract

Pore closure in thick aluminum plate:
from industrial hot rolling to individual pore observation

P. Gravier, F. Mas, A. Barthelemy, E. Boller, L. Salvo, P. Lhuissier

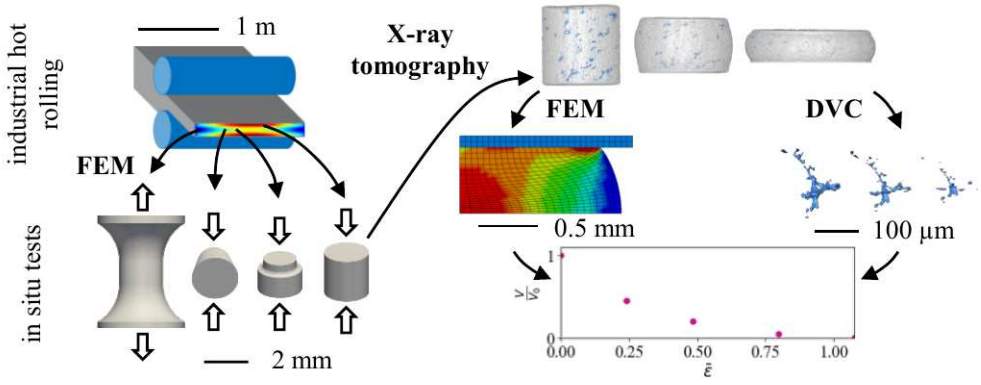

Pore closure in thick aluminum plate: from industrial hot rolling to individual pore observation

P. Gravier[a,b], F. Mas[b], A. Barthelemy[b], E. Boller[c], L. Salvo[a], P. Lhuissier[a,*]

[a] *Université Grenoble Alpes, CNRS UMR5266, Grenoble INP, Laboratoire SIMaP, 38000 Grenoble, France*
[b] *C-TEC Constellium Technology, Centr'Alp 725, rue A. Bergès CS10027, F-38341 Voreppe, France*
[c] *ESRF-The European Synchrotron, CS40220, 38043, Grenoble Cedex 9, France*

Abstract

Pores are often present in large aluminum ingots after casting. To ensure the mechanical reliability of the final thick plates, these pores must be closed during the forming process, hot rolling in the present case. This study aims at understanding the effects of rolling parameters on the volume evolution of pores. To do so, X-ray microtomography is used to track real casting pores during deformation. Nevertheless, thick plates are too large to enable a fine characterization of the evolution of pores during the process. The size and shape of the samples as well as the mechanical boundary conditions must be optimized to meet imaging constraints. This paper focuses on the reproduction of complex loading paths. Multi-scale FE simulations are used to reproduce the loading conditions of thick plate rolling with uniaxial tests on samples of a few millimeters. Uniaxial tests are then characterized with tomography on a synchrotron X-ray beamline. In each sample, tens of pores are individually tracked, giving access to their volume evolution. The local loading path experienced by each pore is determined with FE simulation. It is shown that the volume evolution of a real pore correlates with the hydrostatic integration which is the integral of stress triaxiality along cumulated strain. This confirms that

*Corresponding author
Email address: pierre.lhuissier@simap.grenoble-inp.fr (P. Lhuissier)

the closure of complex casting pores is enhanced by a high relative reduction and high values of L/H ratio during rolling similarly to what was observed numerically on simpler shapes.

Keywords: Aluminum, Hot rolling, FE simulation, in situ X-ray microtomography, Pore volume evolution

---

1. Introduction

Aluminum alloys are largely used in aerospace manufacturing thanks to their low density, their good mechanical properties, and their high resistance to corrosion. Their use as thick plate in aerospace applications depends on the mastery of processing parameters. It is necessary to avoid the presence of pores in the final product and the concomitant deterioration of mechanical properties. Industrially, the soundness of the material is ensured by control tests such as dye penetrant inspection. The number of pores, their size and the distance between pores must be in a certain range. Pores in aluminum products appear during casting. They are caused by the increase of density and the decrease of hydrogen solubility at solidification. In the case of thick aluminum plate, pores are closed by plastic deformation during hot rolling. The optimization of this process is nevertheless complex. There is a large number of relevant rolling parameters (temperature, reduction per pass, roll radius, roll velocity) and their dependence on each other precludes a systematic experimental campaign at the scale of industrial rolling mill. It is essential to accurately describe the closure of pores to ensure the final soundness of the plate.

Park and Yang (1996) showed that pore closure occurs in two steps. First morphology and topology of the pore evolve, along with the pore volume decrease. Then, the internal surfaces of the pore weld together during bounding. In the following, we will only focus on the first step also called mechanical closure. Llanos et al. (2008) investigated pore closure during rolling by using 2D post mortem observations. Such approach allows real pores to be investigated but does not give access to volume evolution. Chen et al. (2011) and later Joo

et al. (2014) used artificial drilled pores in order to track the pore volume evolution during rolling. They found that pore closure is influenced by the reduction of the pass, the pore size and the diameter of the rolls. However, it has been shown numerically by Hwang and Chen (2002) in 2D and by Chen et al. (2010) in 3D that pore shape has a significant effect on pore closure kinetics. Since real pore surrounded by matter cannot be considered as drilled pore, Youssef et al. (2006) and Toda et al. (2009) performed 3D observations of real pores. On the one hand, real complex pores were observed but they were not tracked along the rolling pass schedule. On the other hand, same pores were observed before and after hot rolling. However, in this latter case, only spherical micropores were studied whereas pores in aluminum alloys can have branched and tortuous shapes. Characterization of real complex pores during their closure will allow the understanding of their closure mechanisms and closure kinetics to improve. Then, the current models of pore closure can be validated or improved .

X-ray microtomography offers both a 3D and non destructive characterization at a spatial resolution (order of magnitude of micrometer) compatible with pore description. The non destructive aspect allows several 3D images to be captured per pore during deformation. To save time, sample size was limited to several millimeters. In this way, the whole sample and pores are imaged with sufficient resolution and a unique scan. Such a sample contains several tens of pores, providing many pore volume evolutions to investigate closure kinetics. Samples are deformed at high temperature using a cumbersome setup that requires a synchrotron X-ray source to perform interrupted in situ tests. Consequently, there is significant difference of size between, on the one hand, industrial plate ingots that are hot rolled, which size is about 4m $\times$ 1.5m $\times$ 0.5m, and on the other hand, samples of several millimeters in which pores can be observed. It is necessary to ensure that the loading path experienced by pores during hot rolling can be reproduced with the compression of samples compatible with X-ray microtomography.

In the following, a combination of numerical and experimental approaches is presented. First, finite element simulations are used to compare the loading paths encountered during industrial thick plate rolling to the loading paths encountered during uniaxial tests of small samples with varied shapes. A dedicated experimental setup has been developed to perform high temperature in situ tests characterized by X-ray microtomography. The volume evolution of pores during their deformation are determined using 3D quantitative analysis methods.

2. Numerical and experimental methods

2.1. Numerical simulations

Rolling of industrial plate and a uniaxial mechanical test on a sample compatible with X-ray microtomography differ in terms of sample size and nature of loading. Finite element (FE) simulations were used to ensure that uniaxial tests are representative of the loading states reached with rolling.

Hot rolling simulations are run with LAM3 software (Hacquin, 1996). The model accounts for thermal and mechanical phenomena involved in rolling (such as the deformation of the plate and the rolls, the thermal exchanges between the rolls and the plate, between the plate and the air and the temperature increase in the plate due to mechanical deformation). It couples finite element method to compute the elasto-viscoplastic behavior of the plate and semi-analytic computations of the deformation of the rolls. A stationary Eulerian formulation is used, thus the transient regime at both ends of the plate are not accessible. A classical rolling pass schedule for thick plates requires a progressive reduction of the plate. Several passes between the rolls are necessary to reach the desired final thickness. In the following, we will study the reproduction of the loading state of individual passes. Each pass geometry is usually described by two parameters which are the relative reduction r (Equation 1) and the L/H ratio (Equation 2), where L is the contact length between the rolls and the plate

and H is the mean thickness of the plate. h_1 and h_2 are the entry and exit thicknesses respectively and R_{cyl} is the radius of the rolls (Figure 1).

$$r = \frac{h_1 - h_2}{h_1} \quad \in [0, 1] \tag{1}$$

$$\frac{L}{H} = \frac{2\sqrt{R_{cyl}(h_1 - h_2)}}{h_1 + h_2} \tag{2}$$

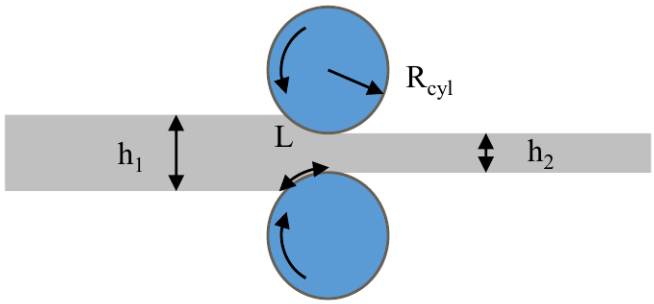

Figure 1: Schematic description of a rolling pass. h_1: entry thickness, h_2: exit thickness, R_{cyl}: radius of the rolls, L: contact length between the rolls and the plate.

FE simulations of uniaxial tests are performed using the software LS-DYNA (LS-DYNA, 2017). Different sample geometries are tested either in compression (cylinder, Brazilian and double-collar) or in tension to broaden the range of accessible loading states (Figure 2). Double-collar geometry was inspired from

the work of Farrugia (2006). For cylinders, double-collars and tension samples, 2D axisymmetric elements are used. For Brazilian tests, 3D hexahedral fully integrated elements are used. The material constitutive equations follow the Sellars-Tegart law (Equation 3) (Sellars and Tegart, 1972).

$$\sigma = \frac{1}{\alpha}\, ln\left(\left(\frac{Z}{A}\right)^{\frac{1}{m}} + \sqrt{\left(\frac{Z}{A}\right)^{\frac{2}{m}} + 1}\right), \quad Z = \dot{\varepsilon}\, exp\left(\frac{Q}{RT}\right) \tag{3}$$

The four parameters α, A, m and Q were determined experimentally using the method described by Zhu et al. (2018). Most of the time, the pores are studied in a matrix following a Norton power law of this type $\dot{\varepsilon} = A\,\sigma^n$. For a given temperature of 480 °C, the Norton index n of the present material is of about 6. Usually, the Norton index of aluminum alloys is between 3 and 10, which limits its effect on pore closure reported by Zhang et al. (2009). Besides, Saby et al. (2015a) observed that the effect of the Norton exponent in this range is negligible compared to the effect of the orientation or the shape of the pore. In the simulation software, the material law consists in several stress-strain curves at different temperatures and strain rates: 10 temperatures between 380 and 580 °C and 10 strain rates between 1×10^{-3} and 1×10^{2} s^{-1}. For compression of cylinders, Brazilians and double-collars, infinitely rigid dies are used in the simulation. A coefficient of static friction of 0.4 between the die and the sample is applied. This coefficient has been chosen in order to match barreling effect that is observed experimentally during compression test. Concerning thermal conditions, the initial temperature is fixed at all sample nodes and no exchanges are considered between the dies and the air. The simulation takes into account the heat due to the mechanical work. Compression tests were simulated up to a relative reduction of 60% and tensile tests up to initiation of necking.

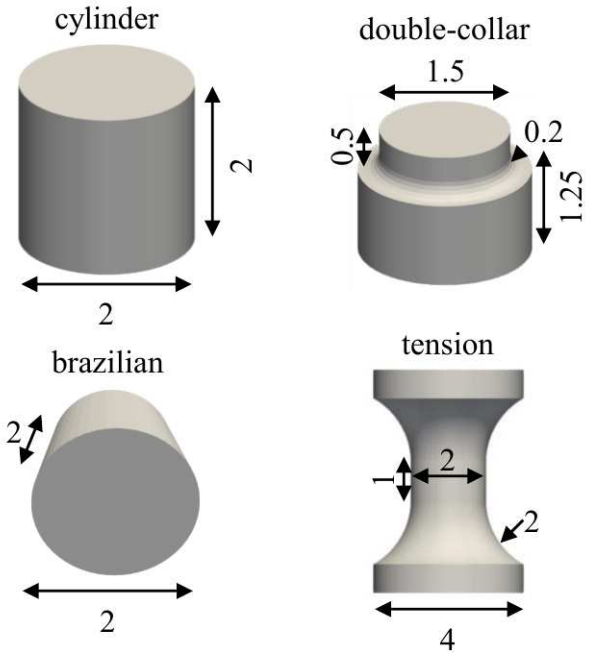

Figure 2: Simulated geometries to investigate loading paths under uniaxial loading. Dimensions are given in millimeters. Loading direction is vertical.

The dimension of pores are small compared to the sample size. It is assumed that the mechanical fields are not modified by the presence of the pores. Therefore, the simulations were performed on samples free of pores. In the literature, cumulated strain (Equation 4) and stress triaxiality (Equation 5) are shown to be the two main mechanical parameters involved in pore closure. They are used in the analytical models of Gurson (1977) and Duva and Hutchinson (1984), the semi-analytical model of Zhang et al. (2009) and the phenomenological model of Saby et al. (2015a). Thus, loading states will first be compared in terms of triaxiality T_X and cumulated strain $\bar{\varepsilon}$.

$$\bar{\varepsilon} = \int_0^t \dot{\bar{\varepsilon}}\, dt \quad \dot{\bar{\varepsilon}} = \sqrt{\frac{2}{3}\, \dot{\underline{\underline{\varepsilon}}} : \dot{\underline{\underline{\varepsilon}}}} \quad \dot{\underline{\underline{\varepsilon}}} = \frac{\partial \underline{\underline{\varepsilon}}}{\partial t} \tag{4}$$

$$T_X = -\frac{p}{\bar{\sigma}} \quad p = -\frac{1}{3}\, tr\left(\underline{\underline{\sigma}}\right) \quad \bar{\sigma} = \sqrt{\frac{3}{2}\, \underline{\underline{\sigma'}} : \underline{\underline{\sigma'}}} \quad \underline{\underline{\sigma'}} = \underline{\underline{\sigma}} + p\underline{\underline{I}} \tag{5}$$

Where $\underline{\underline{\varepsilon}}$ is the strain tensor, $\underline{\underline{\sigma}}$ the stress tensor and p the hydrostatic pressure.

The stress state is more precisely represented considering the Lode parameter μ (Equation 6) in addition to the stress triaxiality.

$$\mu = \frac{2\sigma_2 - \sigma_1 - \sigma_3}{\sigma_1 - \sigma_3} \tag{6}$$

The Lode parameter influence has been mostly studied in the scope of failure of ductile metals. It has been observed by Danas and Ponte Castañeda (2012) that at high triaxiality, ductile failure is controlled by triaxiality but when triaxiality decreases (in absolute value), the Lode parameter plays a significant role. (Zhang et al., 2001) demonstrated that, at low positive triaxiality, the Lode parameter has a non-negligible influence on the pore shape rather than on the pore volume. Chbihi et al. (2017) studied pore closure using FE simulations, they concluded that at low triaxiality, high values of the Lode parameter foster pore closure. More recently, Zhang et al. (2020) and Wang and Dong (2020) proposed two new prediction models of pore closure that incorporate the Lode parameter.

2.2. Experimental data acquisition

A dedicated micropress has been developed (Figure 3.b) to perform in situ mechanical tests at high temperature. The device can perform compression and tensile tests at a controlled speed (up to 1 $mm.s^{-1}$). The applied load is recorded. The sample is placed between the movable piston and the fixed bell (made of boron nitride to be transparent to X-rays) (Figure 3.c). The micropress is mounted on the rotating stage and a furnace is moved down around the bell to heat the sample (Figure 3.a). The furnace is independent from the rotation stage and does not move during the tomography acquisition. Two glassy carbon windows are located on the X-ray path at the entrance and exit of the

furnace.

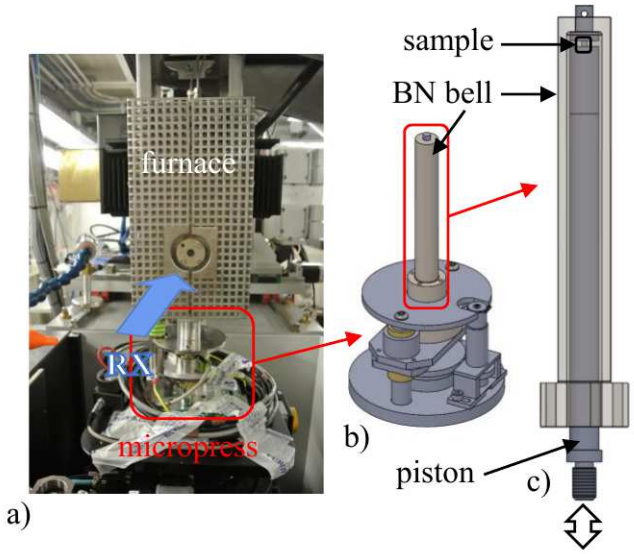

Figure 3: Experimental setup: a) picture of the micropress and the furnace on the ESRF-ID19 beamline. b) Sketch of the micropress. c) Sketch of the upper part of the micropress composed of the bell and the piston surrounding the sample.

In situ tests at high temperature are performed with a synchrotron X-ray source, at the ESRF (European Synchrotron Radiation Facility, Grenoble, France) on ID19 beamline. It provides a parallel quasi-monochromatic coherent X-ray beam with a high flux of photons. A 34 keV X-ray beam energy was used providing projections with a pixel size of 2.44 μm.

To reproduce real rolling conditions, a high piston velocity is used (1 $mm.s^{-1}$). It ensures a strain rate of about $1s^{-1}$. Thus, interrupted in situ tests are performed (Figure 4) with fast tomography acquisition (around 10s for a full scan) to avoid any relaxation problem that might blur images. For each scan,

2000 radiographs of 1536×1440 pixels are recorded using a PCO edge detector mounted on a ×5 optic with a 100 µm thick YAG scintillator. Reconstructions are performed with the software PyHST (High Speed Tomography in python version) (Mirone et al., 2014) using a phase contrast resolution with an approach developed by Paganin et al. (2002) and filtered backprojection. Ring artifacts are removed with an in house ESRF Matlab script on reconstructed volumes (Lyckegaard et al., 2011).

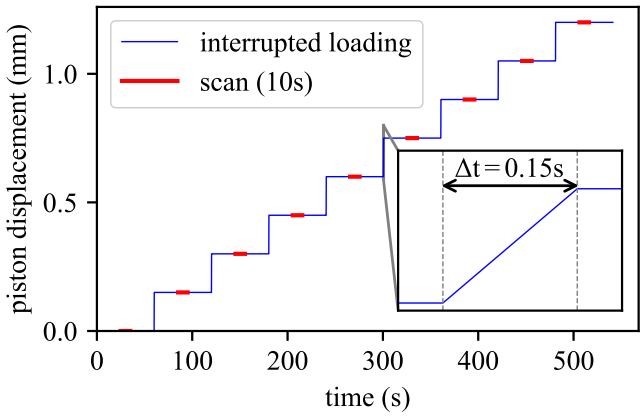

Figure 4: Displacement of the die as a function of time for an interrupted compression in 8 steps of 150 μm at 1 $mm.s^{-1}$.

A total of 18 samples have been tested with different geometries (11 cylinders, 4 double-collars, 2 Brazilians and 1 tensile test). For cylinders, different temperature (from 430 to 520°C), compression speeds (from 0.1 to 1 $mm.s^{-1}$) and alloys have been tested (2XXX and 7XXX series).

2.3. Data processing and tracking method

Three phases are distinguishable in the tomographic data: pores, matrix and intermetallics (as visible in Figure 5). Image processing involving filters and thresholding is used to isolate the pores (with ImageJ software (Schneider et al., 2012)). Two consecutive backgrounds were subtracted from the image.

The first one is generated using a 2D mean filter with a radius of 20 voxels. It allows pores to be detected and to fill them to generate a second 2D mean background with a radius of 10 voxels. Then pore thresholding is performed using a cutoff value kept constant for all the samples. In the following, only pores with a volume higher than 8 voxels (or 116 μm^3) will be considered.

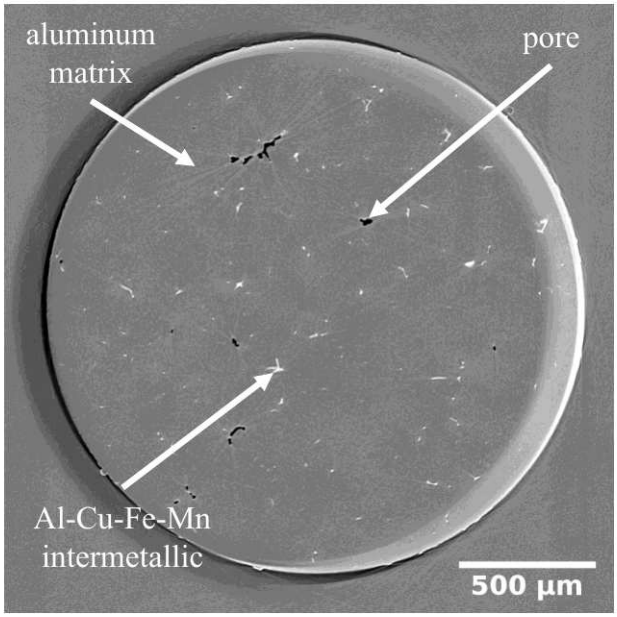

Figure 5: Visible phases in a cross section of a cylindrical sample after reconstruction: pores (dark), intermetallics (bright) and the matrix (medium grey).

The interest of in situ tests is to follow the morphological evolution of pores during sample deformation. However, pores tracking from one scan to another is not straightforward due to the large number of pores (several tens), the large and heterogeneous deformation of the sample and the topological evolution of pores (fragmentation, change of shape). Hence, an automatic procedure has been developed by Lhuissier et al. (2021) to track pores all along the deforma-

tion. This procedure based on Digital Volume Correlation (DVC), provides an estimate of the displacement field thanks to the tracking of intermetallics. The interpolation of the displacement field allows to track pores.

The local mechanical field is obtained thanks to FE numerical simulation with LS-DYNA. The boundary conditions applied as well as the sample shape for the simulation are based on the in situ experiments: real sample shape is used and measured displacement of dies is applied.

All in all, 18 samples have been scanned with a total of 158 scans. The data processing workflow has been automated to get reliable and comparable data from one scan to another (Figure 6). Image processing and DVC give access to the morphological evolution of every pore in every sample during the compression or tensile tests. Coupling with simulation, which provides local loading path, it is possible to access individual pore closure or opening kinetics, meaning the relationship between morphological evolution and local loading conditions. An example of such evolution is given in Figure 6 with the pore volume change as a function of cumulated strain.

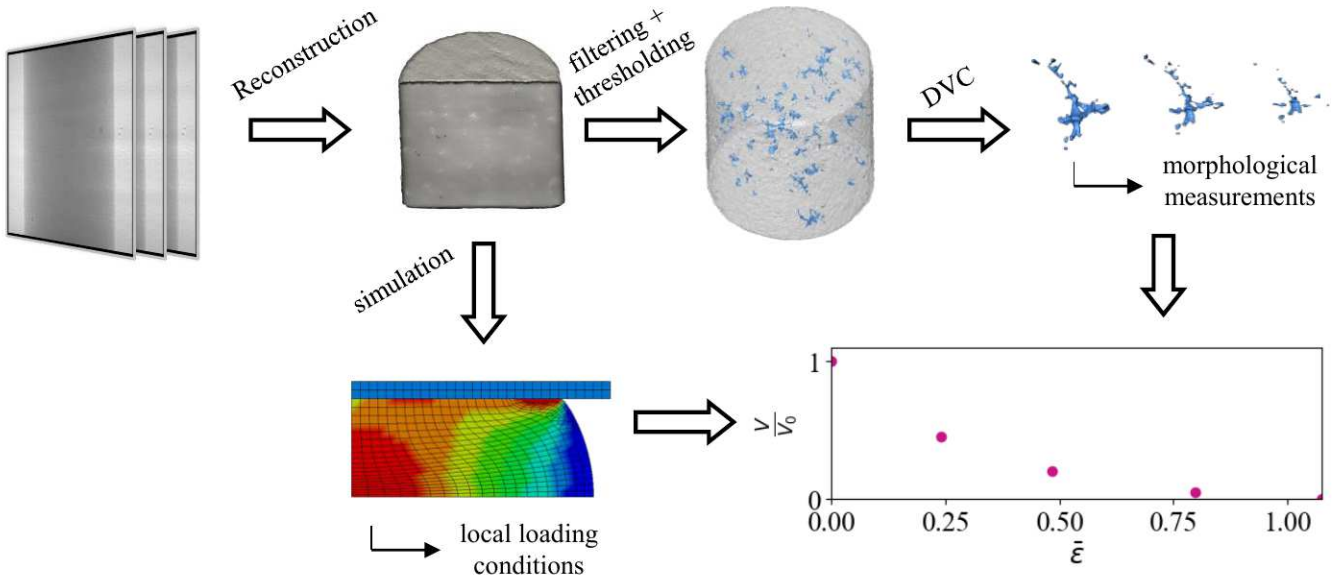

Figure 6: Processing workflow to obtain the pore closure kinetics from radiographs acquired with tomography.

3. Results and discussions

3.1. Loading paths during hot rolling

During hot rolling, thermo-mechanical fields are not homogeneous in the transverse section of the plate (section perpendicular to the rolling direction). Figure 7 presents the distribution of hydrostatic pressure within the section located right between the rolls. The thickness is the dimension of the plate along Short-Transverse (ST) direction. The width is along Long-Transverse (LT) direction. High hydrostatic pressure is reached close to the rolls at the mid-width while low hydrostatic pressure is reached on the edges at mid-thickness. In this area of negative hydrostatic pressure, pores will tend to open. Thus, loading path is highly dependent on the considered position in the transverse section.

Mechanical fields at five representative positions in the plate are studied (positions marked on Figure 7). The *center* position is located at mid-width and mid-thickness. Two other positions are studied along mid-width: the *surface* position which is in contact with the rolls and the *quarter thickness* position which is initially (i.e. before rolling) at mid-way between *center* and *surface* positions. Along mid-thickness, *extreme edge* position is at the side surface of the plate and *edge* position is where the hydrostatic pressure reaches lowest values during rolling.

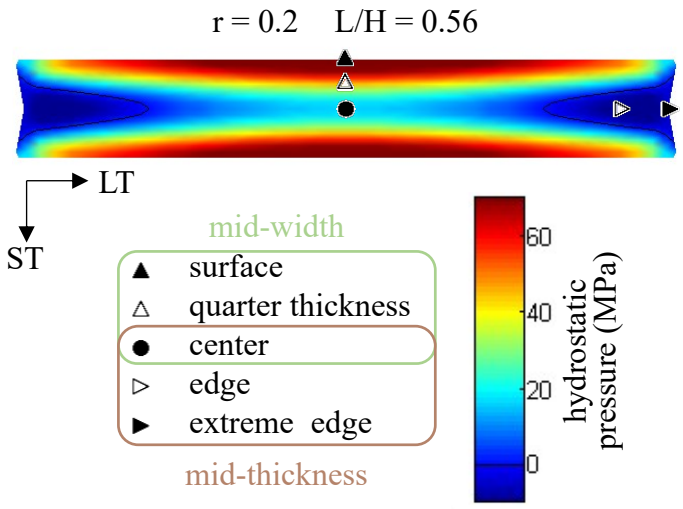

Figure 7: Distribution of hydrostatic pressure within the transverse section between the rolls.

Several rolling pass schedules are simulated changing: the reduction per pass, the roll radii, the temperature, and the roll speed. Each pass is studied individually, independently of the previous or following passes. Loading paths are defined as the local evolution of stress triaxiality as a function of the cumulated strain. Figure 8.a shows, for a given pass (r=0.2 and L/H=0.56), the different loading paths depending on the position in the plate. Close to the edges (*edge* and *extreme edge*), tensile state, with positive triaxiality, appears. At mid-width (*center* and *quarter thickness*) loading state is more compressive and strain increases towards the rolls (*quarter thickness*). Regardless to the position, the triaxiality as a function of the cumulated strain is almost constant. Loading paths can be approximated as the final loading state using two descriptors: the final cumulated strain $\bar{\varepsilon}_f$ (i.e. cumulated strain reached locally at the end of the pass) and the average triaxiality $\langle T_X \rangle_f$ (Equation 7).

$$\langle T_X \rangle_f = \frac{1}{\bar{\varepsilon}_f} \int_0^{\bar{\varepsilon}_f} T_X \, \mathrm{d}\bar{\varepsilon} \tag{7}$$

Each considered position in the plate has an influence on both $\bar{\varepsilon}_f$ and $\langle T_X \rangle_f$. For a given position, an increase of relative reduction r results in an increase of

final cumulated strain (Figure 8.b). The triaxiality is directly linked to the L/H ratio. Higher values of L/H lead to more compressive states (Figure 8.c). These results are consistent with the observations of Wallerö (1985) who recommends large values of relative reduction and L/H ratio to favor pore closure. No effect of rolling temperature nor roll speed was found on the loading states.

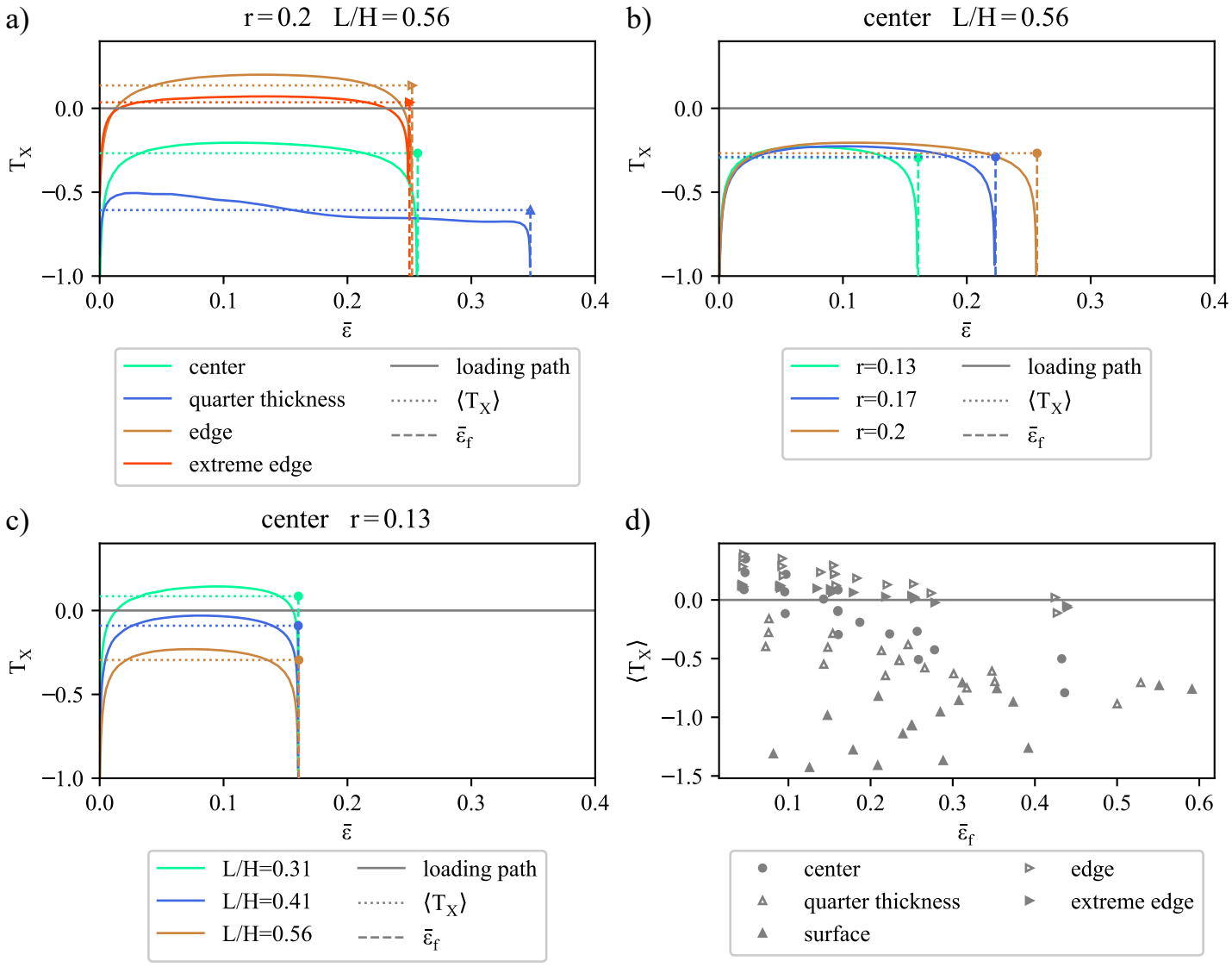

Figure 8: a-c) Effect of different parameters on the loading paths of a single rolling pass: a) position in the transverse section, b) relative reduction value, c) L/H ratio value. d) Loading states of rolling to be reproduced.

Figure 8.d shows the loading states at different positions for passes of different pass schedules that could be used for industrial hot rolling. It defines a

map of loading states that have to be reproduced with uniaxial tests. Three zones can be distinguished when focusing on the triaxiality: i) the edge, the extreme edge and the center for low deformation where $\langle T_X \rangle \geq 0$; ii) the quarter thickness and the center for large deformation where $0 > \langle T_X \rangle \geq -0.7$; iii) the surface of the plate where $\langle T_X \rangle < -0.7$.

Similarly to the stress triaxiality, the Lode parameter along cumulated strain is almost constant (Figure 9.a). For each pass, the Lode parameter path can be locally approximated by the mean Lode parameter and the final cumulated strain. Figure 9.b shows the results for a pass schedule of 5 passes.

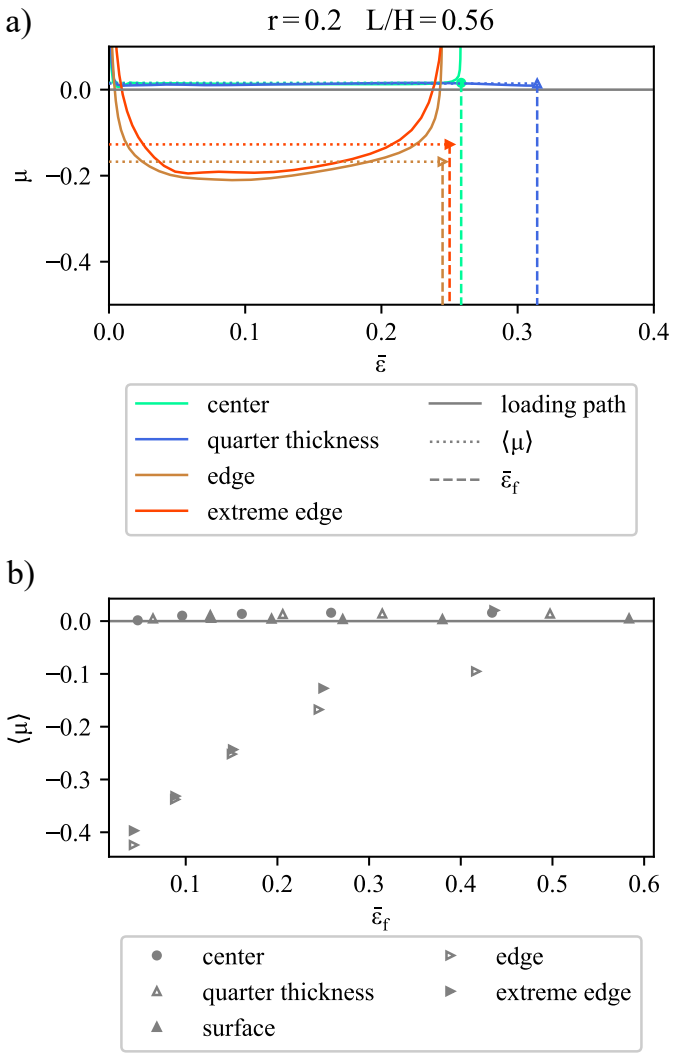

Figure 9: a) Effect of the position on the Lode parameter path b) Lode parameter values obtained for 5 different passes of rolling at different positions in the plate.

When looking at the Lode parameter, two zones are distinguished. Away from the edge, the Lode parameter is zero. This value results from the plane stain state. Thus, in most of the plate variations of pore closure kinetics are not influenced by the Lode parameter which is constant. Close to the edges, the

plane strain state is not fulfilled and the Lode parameter takes negative values. Its absolute value decreases when the cumulated strain increases. Besides, these zones experience low triaxiality (in absolute value). In that case, either in tension or in compression, Zhang et al. (2001) and Wang and Dong (2020) observed that the Lode parameter has an influence on the pore volume evolution. They also observed that the Lode parameter affects the evolution of the pore shape when observing spherical or ellipsoidal pores. However, in our present case, we want to study real casting pores which have complex shapes. Most of them are tortuous and branched. Contrary to ellipsoid, the shape of a real pore cannot be described with a few number of parameters for which we can determine the sensibility to the Lode parameter. Thus, the evolution of volume due to the modification of the pore shape will depend on the Lode parameter value but also on the initial shape of the pore.

Considering both stress triaxiality and Lode parameter to describe the stress states encountered during rolling, we can identify three different zones:

- The edge of the plate (edge and extreme edge positions) and the center of the plate for low deformation where $\langle T_X \rangle \geq 0$ and $\langle \mu \rangle \leq 0$.
- The center of the plate for high deformation and the quarter thickness where $0 > \langle T_X \rangle \geq -0.7$ and $\langle \mu \rangle = 0$.
- The surface where $\langle T_X \rangle < -0.7$ and $\langle \mu \rangle = 0$.

3.2. Loading paths during in situ tests

Simulations are performed to determine the loading states accessible with uniaxial mechanical tests on small samples. The objective is to find sample geometries that cover the entire map of loading states previously defined (Figure 8.d).

The loading states of uniaxial tests can be compared to those of rolling using the mean triaxiality and the cumulated strain at the end of deformation. However, it is not relevant to do so since the final cumulated strain only depends

on the total displacement of the dies imposed during the test. For example, in compression (Figure 10.a), at the center of the cylinder, the final strain reaches a higher value than for a single rolling pass (2 versus 1.2). Nevertheless, all intermediate cumulated strain values up to the final value give access to many mean triaxiality ratios because triaxiality is not constant during deformation for uniaxial tests. Thus, for each sample, the accessible loading states are represented by the envelope of all the loading paths $\langle T_X \rangle = f(\bar{\varepsilon})$ of all the elements of the sample. Note that loading paths described as $\langle T_X \rangle = f(\bar{\varepsilon})$ are slightly different from those described by $T_X = f(\bar{\varepsilon})$. Figure 10 shows this envelope for the different sample geometries.

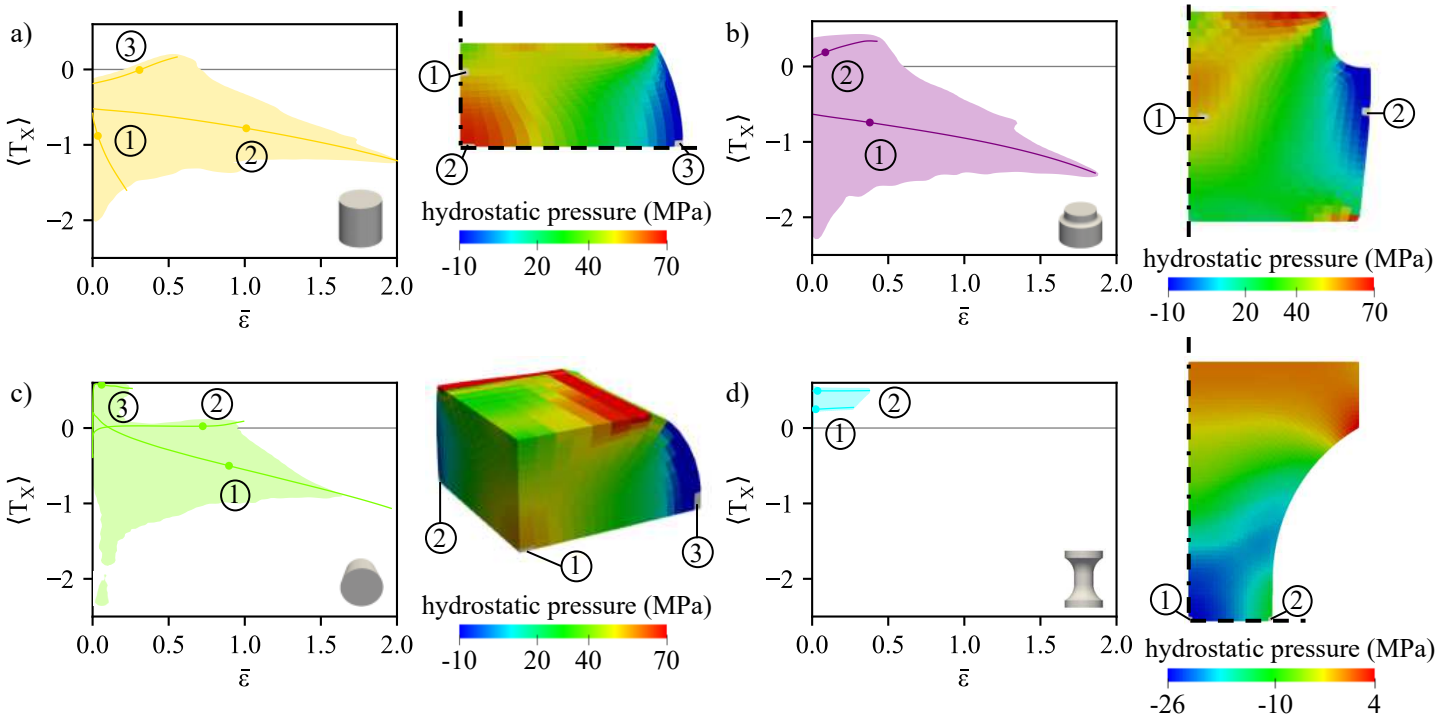

Figure 10: Loading domains and local triaxiality for the uniaxial tests: a) compression of a cylinder, b) compression of a double-collar, c) Brazilian compression of a cylinder, d) tension of a notched sample.

On the same Figure, local loading paths of some chosen elements are repre-

sented by lines. As for rolling, the loading path depends on the location within the sample. During the compression of a cylinder (Figure 10.a), higher cumulated strains are reached at the center of the sample with negative triaxiality (in element 2). Triaxiality reaches positive values close to the border (in element 3) after a local cumulated strain of 0.5. Tensile stresses appear due to the barrel shape induced by friction between the dies and the sample. Close to the dies (in element 1), strain is low. During the compression of a cylinder along its axis, a very limited volume endures loading states with triaxiality ratios larger than or even close to 0. Simulations with different alloys, temperatures and compression speeds have not shown significant effects on loading paths.

Figure 10.b presents the loading domain for Brazilian tests. Large strains at triaxiality close to zero are accessible in the elements at the center of the cylinder base (in element 2). Tension due to the barrel effect is accentuated during the test. High triaxiality ratios are reached, like in element 3, but strain remains low.

Results for the simulations for double-collar samples are given in Figure 10.c. For double-collar geometries, the upper part of the sample acts as an indent for lower part. This results in positive triaxiality ratios even at early stage of deformation.

Finally, with the tensile test presented on Figure 10.d positive triaxiality ratios of about 0.33 can be reached with a low dispersion on loading paths. With this geometry, there is no need to consider elements at the border of the specimen to access positive stress triaxiality ratios.

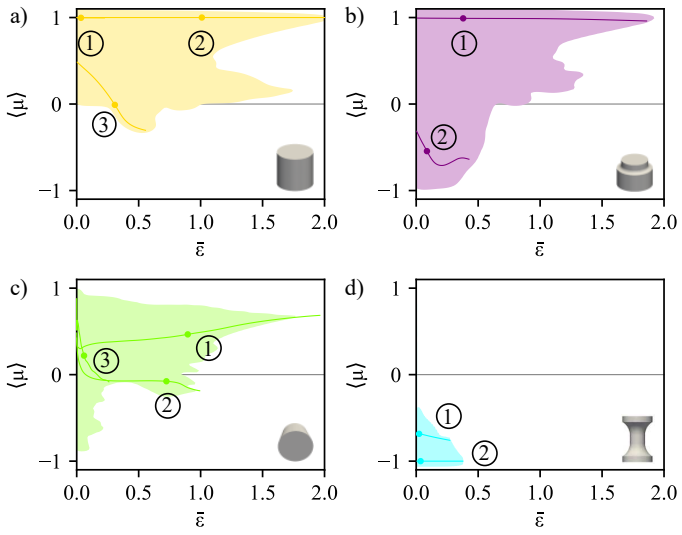

Figure 11: Loading domains and local Lode parameter for the uniaxial tests: a) compression of a cylinder, b) compression of a double-collar, c) Brazilian compression of a cylinder, d) tension of a notched sample. The local paths are those of elements presented on Figure 10.

Figure 11 presents the evolution of the Lode parameter during uniaxial tests. For deformation in compression (Figure 11.a-c) the value of the Lode parameter is mostly between $\langle\mu\rangle = 0$ (representative of plane strain) and $\langle\mu\rangle = 1$ (representative of uniaxial stress). With the compression of a cylinder or a double-collar, it is possible to reach negative values for the Lode parameter, in the elements close to the border of the sample. For the tensile test the Lode parameter is close to -1 which is representative of uniaxial tension.

In conclusion, the three loading zones of rolling previously described can be reproduced with uniaxial tests:

- At the edge of the plate (edge and extreme edge positions) and the center of the plate at low deformation $\langle T_X\rangle \geq 0$ and $\langle\mu\rangle \leq 0$. Both ranges of the Lode parameter and triaxiality are reproduced by the tensile test and also in zones close to the edges in compression of the cylinder, the double-collar and the Brazilian test.

- At the center of the plate at high deformation and the quarter thickness $0 > \langle T_X \rangle \geq -0.7$ and $\langle \mu \rangle = 0$. The range of triaxiality is reproduced by the different types of compression tests. There is a variability of the Lode parameter between 1 and 0 in those samples. Chbihi et al. (2017) found that for a given pore at $\langle T_X \rangle = -0.33$, the closure strain is 0.6 at $\langle \mu \rangle = 1$ and it is 0.75 for $\langle \mu \rangle = 0$. On the other hand, Saby et al. (2015a) observed that the closure strain varies by twice on ellipsoids when different orientations or shape factors are considered (for $\langle T_X \rangle = -0.33$). In the present case of real casting pores with various orientations and shapes, the effect of the Lode parameter in this range of triaxiality will be of second order compared to the effect of morphology. For this zone we will only focus on the reproduction of triaxiality.

- At the surface $\langle T_X \rangle < -0.7$ and $\langle \mu \rangle = 0$. The triaxiality is highly negative, the closure is controlled by the value of the triaxiality and the Lode parameter has a negligible effect. Such loading conditions are fulfilled at the center of the sample under uniaxial compression.

The combination of the different geometries of uniaxial tests enables to reach all the final loading states of rolling. Note that this study gives all the accessible loading states in in situ samples, however, experimentally pores are not present in every element of every sample. Thus, it is necessary to perform several tests with the same sample geometry to increase the chance to have pores in regions of interest.

3.3. Example of experimental results

Figure 12 shows the experimental results for a double-collar sample, with the 3D evolution of pores within the sample (Figure 12.a). The relative reduction (r) is computed with the initial and current height of the sample (it is not linked to that of rolling). The strain is inhomogeneous in the sample, the upper part of the sample with a smaller radius deforms more and deformation is progressively

transmitted to the lower part. In consequence, pores start to close in the upper part of the sample and closure propagates to the lower part close to the axis of symmetry whereas pores close to the border evolve less. Sample geometry used for simulation is shown on Figure 12.b. It is generated from measurement on tomographic volume and thus differs from geometries previously simulated. We can observe several tens of pores in the sample. Figure 12.c shows the loading paths of two clusters of pores together with their morphological evolution. Loading path is obtained with simulation and morphological evolution thanks to DVC. Cluster A which experiences a triaxiality close to zero has few changes in shape whereas cluster B that is subjected to higher negative triaxiality and higher cumulated strain progressively closes.

Such results are accessible for all the pores in all the tested samples. Thus, closure kinetics of real pores with large ranges of triaxiality and cumulated strain, comparable to those of hot rolling, can be studied.

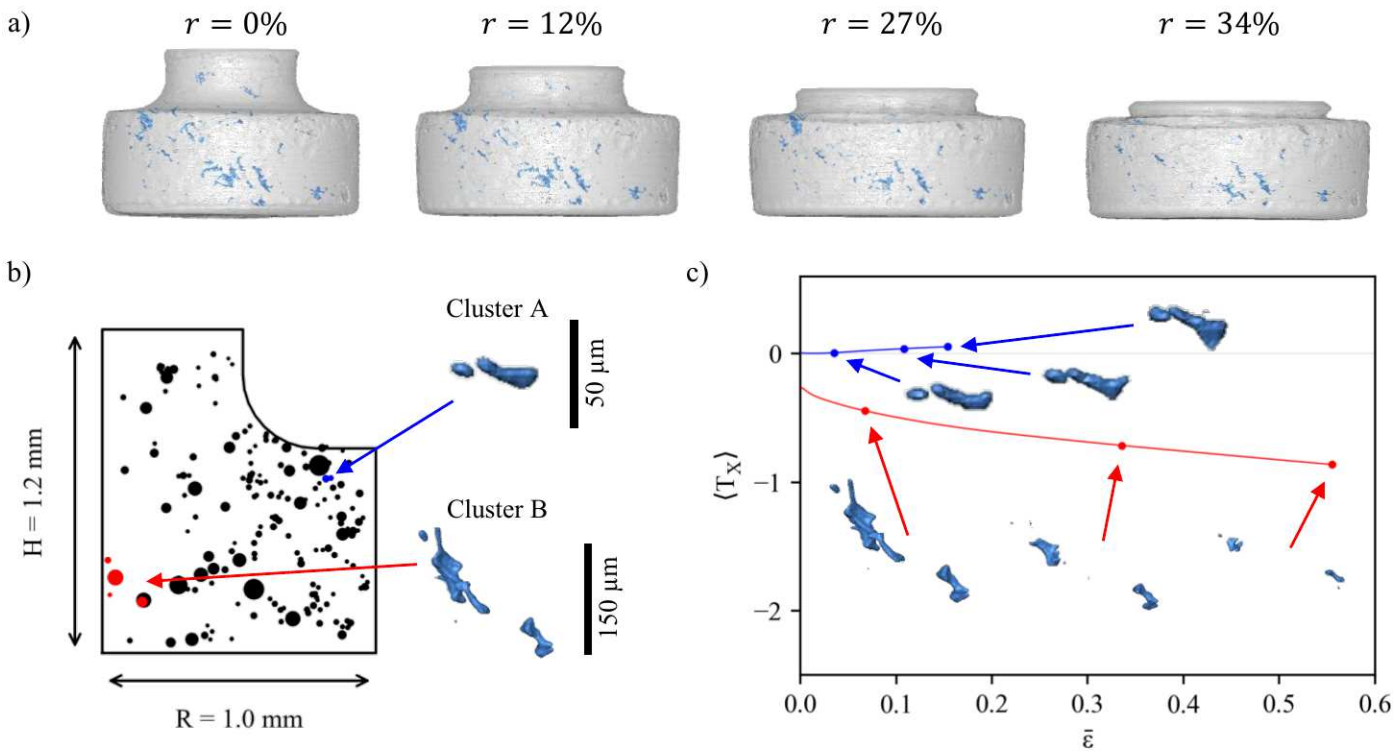

Figure 12: Experimental results of the volume evolution of pores in a double-collar sample. a) 3D rendering of the pores (in blue) in the sample during compression. b) Initial state: schematic representation of all the pores (pores are represented by black points with a diameter equal to the pore equivalent diameter, they are projected in the axisymmetric geometry used for simulation) and 3D rendering of two clusters of pores. c) Loading path and morphological evolution of the two considered clusters.

3.4. On the choice of loading paths descriptors

The hydrostatic integration (noted Q in Equation 8) is often used to describe pore closure, as reviewed by (Saby et al., 2015b). It is equal to the product of the two loading state descriptors chosen before, namely the average triaxiality and the cumulated strain. The hydrostatic integration takes into account the variation of triaxiality during the test and it is computed locally to account for the inhomogeneities of mechanical fields in the sample.

$$Q(\bar{\varepsilon}) = \int_0^{\bar{\varepsilon}} T_X(\bar{\varepsilon}) d\bar{\varepsilon} = \langle T_X \rangle \, \bar{\varepsilon} \tag{8}$$

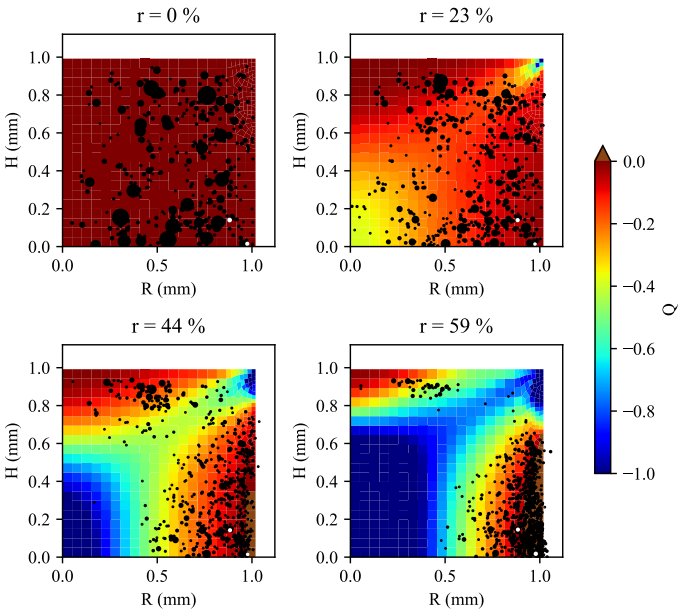

Figure 13: Superposition of the hydrostatic integration field Q and the pores present in a cylindrical sample during its compression. Pores are represented by black points with a diameter equal to the pore equivalent diameter. Everything is represented in the initial state geometry and in the axisymmetric plane, taking into account the axial and planar symmetries of the cylinder. In white, tracking of two pores in zone of low $|Q|$.

Figure 13 shows the qualitative correlation between the hydrostatic integration and the evolution of the volume of real pores. The colored background rep-

resents the hydrostatic integration field. Pores are represented by black points of equivalent diameters (meaning that the point diameter is equal to the pore equivalent diameter). Hydrostatic integration field and pores are represented in the initial configuration. Along deformation, hydrostatic integration decreases in most of the sample. On the edge, positive values progressively appear, between $r = 23\%$ and $r = 44\%$, due to the barrel shape induced by the friction between the dies and the sample. Close to the surface in contact with the die, hydrostatic integration remains low due to low strain. Conversely, in the upper right corner Q decreases with average strain because the lateral surface of the cylinder progressively comes into contact with the die leading to large strains.

Hydrostatic integration variations correlate well with pore volume variations. When Q is positive, pores grow and new pores nucleate whereas they shrink where Q is negative and shrinkage is more pronounced where the absolute value of Q is high. Contrary to what Nakasaki et al. (2006) and Kakimoto et al. (2010) stated, pores are still present when $Q < -0.2$ and even for lower values. Here, pores are totally closed for values around $Q = -1$.

The good qualitative correlation between the hydrostatic integration and the pore shrinkage or growth shows that mean triaxiality and cumulated strain are relevant descriptors to focus on in order to reproduce loading paths.

4. Conclusions

In situ mechanical tests characterized by X-ray microtomography can be used to acquire experimental data on real pore volume evolution under deformation representative of hot rolling. Nevertheless, this method requires small samples (with dimensions of a few millimeters) whereas industrial rolling involves plates at the meter scale. To ensure that the loading states accessible with uniaxial tests are representative of the loading states of rolling, FE simulations of both industrial rolling at the meter scale and uniaxial tests at the millimeter scale were performed. The loading states that can be experienced

by pores in terms of triaxiality and cumulated strain were compared. Based on these simulations, the following conclusions can be drawn:

- When a single pass of rolling is considered, the use of the mean triaxiality during deformation and the final cumulated strain gives a good approximation of the local loading state experienced during the pass. Their values depend on the considered position in the plate. The relative reduction of the pass has a direct influence on the cumulated strain and the triaxiality value is linked to the L/H ratio.

- The combination of several sample geometries deformed uniaxially allows all the loading states experienced during thick plate hot rolling to be reproduced. Selected tests are: compression of a cylinder along its axis, Brazilian test, double-collar compression and tensile test on a notched sample. In cases where the Lode parameter affects pore volume evolution, for low absolute values of triaxiality, those geometries also reproduce the ranges of values of the Lode parameters encountered during rolling.

- A dedicated sample environment integrated within a synchrotron beamline was developed to capture samples evolution during interrupted in situ tests at high temperature with X-ray microtomography. An automated data processing workflow combining images processing, DVC and FE simulation was set up. It allows the morphological evolution of each pore to be linked to the local mechanical fields it experiences during the deformation.

- The average triaxiality $\langle T_X \rangle$ and cumulated strain $\bar{\varepsilon}$ have been used to compare loading paths encountered during rolling and during uniaxial tests. This choice is justified by a qualitative comparison of the hydrostatic integration field, combining both parameters, and the locations where pores shrink or grow.

- From the volume evolution of pores with the hydrostatic integration, it can be deduced that pores closure is enhanced by high cumulated strain

and high negative triaxiality. They can be reached during rolling with a high relative reduction and high values of L/H ratio.

Thus, with the method described in this article, experimental data on the evolution of real pores are acquired during loading representative of hot rolling. For the sake of clarity, the conclusions on pore closure are limited in this paper. Nevertheless, this method can have many applications. It could be used, on the one hand, to obtain a better description of pore closure or opening kinetics by studying pore volume evolution as a function of the hydrostatic integration. It also gives access to fine morphological evolution in 3D during deformation which will allow mechanisms involved in pore closure or opening to be studied. Finally, the database of hundreds of pores could be used to test the different models of pore volume evolution available in the literature.

Acknowledgments

The authors would like to thank the Association Nationale Recherche Technologie (ANRT) and Constellium Technology Center (C-TEC) for funding the project. The European Synchrotron Radiation Facility (ESRF) is gratefully acknowledged for offering beam-time associated to the MA3482 proposal. Thanks to Gary Admans for proofreading the article.

References

Chbihi A, Bouchard PO, Bernacki M, Pino Muñoz D. Influence of Lode angle on modelling of void closure in hot metal forming processes. Finite Elements in Analysis and Design 2017;126(September 2016):13–25.

Chen J, Chandrashekhara K, Mahimkar C, Lekakh SN, Richards VL. Void closure prediction in cold rolling using finite element analysis and neural network. Journal of Materials Processing Technology 2011;211(2):245–55.

Chen Kb, Yang Y, Liu K, Shao G. Simulation of void defect evolvement during the forging of steel ingot. Advanced Materials Research 2010;97-101:3079–84.

Danas K, Ponte Castañeda P. Influence of the Lode parameter and the stress triaxiality on the failure of elasto-plastic porous materials. International Journal of Solids and Structures 2012;49(11-12):1325–42.

Duva J, Hutchinson J. Constitutive potentials for dilutely nonlinear materials. Chemical Physics 1984;3(July):228–34.

Farrugia DCJ. Prediction and avoidance of high temperature damage in long product hot rolling. Journal of Materials Processing Technology 2006;177:486–92.

Gurson AL. Continuum Theory of Ductile Rupture by Void Nucleation and Growth: Part I—Yield Criteria and Flow Rules for Porous Ductile Media. Journal of Engineering Materials and Technology 1977;99(1):2.

Hacquin A. Modelisation thermomecanique tridimensionnelle du laminage couplage bande/cylindres. Ph.D. thesis; Ecole Nationale Supérieure des Mines de Paris; 1996.

Hwang YM, Chen DC. Finite element simulations on void closure behaviour inside the sheet during sheet rolling processes. Proceedings of the Institution of Mechanical Engineers, Part B: Journal of Engineering Manufacture 2002;216(9):1227–37.

Joo Sh, Jung J, Chun MSIK, Moon CHO, Lee S, Kim HS. Finite Element and Experimental Analysis of Closure and Contact Bonding of Pores During Hot Rolling of Steel. Metallurgical and Materials Transactions A: Physical Metallurgy and Materials Science 2014;45(8):4002–11.

Kakimoto H, Arikawa T, Takahashi Y, Tanaka T, Imaida Y. Development of forging process design to close internal voids. Journal of Materials Processing Technology 2010;210(3):415–22.

Lhuissier P, Bormann T, Pelloux G, Bataillon X, Pelloux F, Josserond C, Gravier P, Blandin JJ, Boller E, Salvo L. High temperature deformation

followed in situ by X-ray micro-tomography: A methodology to track features under large strain. Journal of Synchrotron Radiation 2021;.

Llanos JM, Santisteban V, Demurger J. Improvement of central soundness in long products from a through process control of solidification and reheating and rolling. Technical Report; European Commission - Research Fund for Coal and Steel; 2008.

LS-DYNA . LS-DYNA R9.1.0. `http://www.lstc.com/products/ls-dyna`; 2017.

Lyckegaard A, Johnson G, Tafforeau P. Correction of Ring Artifacts in X-ray Tomographic Images. International Journal of Tomography & Statistics 2011;18(F11):10.

Mirone A, Brun E, Gouillart E, Tafforeau P, Kieffer J. The PyHST2 hybrid distributed code for high speed tomographic reconstruction with iterative reconstruction and a priori knowledge capabilities. Nuclear Instruments and Methods in Physics Research Section B: Beam Interactions with Materials and Atoms 2014;324:41–8.

Nakasaki M, Takasu I, Utsunomiya H. Application of hydrostatic integration parameter for free-forging and rolling. Journal of Materials Processing Technology 2006;177(1-3):521–4.

Paganin D, Mayo SC, Gureyev TE, Miller PR, Wilkins SW. Simultaneous phase and amplitude extraction from a single defocused image of a homogeneous object. Journal of Microscopy 2002;206(1):33–40.

Park C, Yang D. A study of void crushing in large forgings I: Bonding mechanism and estimation model for bonding efficiency. Journal of Materials Processing Technology 1996;57(1-2):129–40.

Saby M, Bouchard PO, Bernacki M. A geometry-dependent model for void closure in hot metal forming. Finite Elements in Analysis and Design 2015a;105:63–78.

528 Saby M, Bouchard PO, Bernacki M. Void closure criteria for hot metal forming:
529 A review. Journal of Manufacturing Processes 2015b;19(2):239–50.

530 Schneider CA, Rasband WS, Eliceiri KW. NIH Image to ImageJ: 25 years of
531 image analysis. Nature Methods 2012;9(7):671–5.

532 Sellars C, Tegart WM. Hot workability. International Metallurgical Reviews
533 1972;17(1):1–24.

534 Toda H, Minami K, Koyama K, Ichitani K, Kobayashi M, Uesugi K, Suzuki
535 Y. Healing behavior of preexisting hydrogen micropores in aluminum alloys
536 during plastic deformation. Acta Materialia 2009;57(15):4391–403.

537 Wallerö A. Closing of a central longitudinal pore in hot rolling. Journal of
538 Mechanical Working Technology 1985;12(2):233–42.

539 Wang X, Dong X. A void evolution model accounting for stress triaxiality, Lode
540 parameter and effective strain for hot metal forming. International Journal
541 of Mechanical Sciences 2020;168(November 2019).

542 Youssef YM, Chaijaruwanich A, Hamilton RW, Nagaumi H, Dashwood RJ,
543 Lee PD. X-ray microtomographic characterisation of pore evolution during
544 homogenisation and rolling of Al–6Mg. Materials Science and Technology
545 2006;22(9):1087–93.

546 Zhang K, Bai J, François D. Numerical analysis of the influence of the Lode
547 parameter on void growth. International Journal of Solids and Structures
548 2001;38(32-33):5847–56.

549 Zhang Q, Niu L, Liang Z, Cao M, Zhou T. A porosity closure model consid-
550 ering stress triaxiality ratio and Lode stress parameter. Journal of Materials
551 Processing Technology 2020;286(May):116824.

552 Zhang XX, Cui ZS, Chen W, Li Y. A criterion for void closure in large ingots dur-
553 ing hot forging. Journal of Materials Processing Technology 2009;209(4):1950–
554 9.

555 Zhu Rh, Liu Q, Li Jf, Chen Yl, Zhang Xh, Zheng Zq. Flow curve correction
556 and processing map of 2050 Al–Li alloy. Transactions of Nonferrous Metals
557 Society of China 2018;28(3):404–14.